

CHANGES OF MAGNETIC STRUCTURE IN THREE DIMENSIONS ASSOCIATED WITH THE X3.4 FLARE OF 2006 DECEMBER 13

JU JING,^{1,2} THOMAS WIEGELMANN,³ YOSHINORI SUEMATSU,⁴ MASAHITO KUBO,⁵ AND HAIMIN WANG^{1,2}

Received 2007 December 3; accepted 2008 February 5; published 2008 March 6

ABSTRACT

Recent observations demonstrated that sunspot structure can change rapidly and irreversibly after flares. One of the most puzzling results is the increase in magnetic shear around the flaring magnetic polarity inversion line after flares. However, all these observations were made at the photosphere level. In this Letter, we study the altitude variation of the nonpotentiality of the magnetic fields associated with the 4B/X3.4 flare of 2006 December 13. The vector magnetograms with unprecedented quality from *Hinode* before and after the flare are used as the boundary conditions to extrapolate the three-dimensional nonlinear force-free magnetic fields and the potential fields. The former are computed with the optimization algorithm and the latter with the Green's function method. At the photosphere boundary, magnetic shear increases after the flare in a local area close to the flaring magnetic polarity inversion line. Two measures of the magnetic nonpotentiality, the weighted mean shear θ_w and the total magnetic shear $\theta_w B$, are calculated in this area at progressively higher altitude. By comparing their altitude variation profiles before and after the flare, we find that the nonpotentiality of the local area increases after the flare below ~ 8 Mm and decreases from that height to ~ 70 Mm. Beyond 70 Mm, the magnetic fields approach potential for both times.

Subject headings: Sun: activity — Sun: corona — Sun: flares — Sun: magnetic fields

1. INTRODUCTION

There is mounting evidence of the rapid and permanent changes of photospheric magnetic fields during major flares (Wang 1992, 2006; Wang et al. 1994; Kosovichev & Zharkova 2001; Sudol & Harvey 2005). In particular, with white-light (WL) observations obtained from the *Transition Region and Coronal Explorer (TRACE)*, a consistent pattern of changes in sunspot structures has been identified: part of the penumbral segments in the outer δ -spot decays rapidly during flares, and meanwhile, the umbral cores and/or inner penumbral regions are enhanced (Wang et al. 2004; Deng et al. 2005; Liu et al. 2005; Chen et al. 2007). To explain these observations, Liu et al. (2005) proposed a reconnection picture in which the two components of a δ -spot become strongly connected during the flare. The penumbral fields change from a highly inclined to a more vertical configuration, which leads to the penumbral decay. Wang (2006) favored the model of tether cutting (Moore et al. 2001 and references therein) via magnetic reconnection at or close to the photosphere.

Among these flare-associated changes in the photospheric magnetic field, the most intriguing result is that magnetic shear around the flaring magnetic polarity inversion line (PIL) may actually increase after flares (e.g., Ambastha et al. 1993; Chen et al. 1994; Wang et al. 1994), which indicates energy buildup, rather than release. This result poses a difficulty in explaining the contradiction between the observed increase in magnetic shear and the requirement to release magnetic energy to power

the flares. However, previous observations were made at the photosphere level, which is the only environment in which we can directly observe and measure the solar magnetic field. To better understand the role that magnetic fields play in powering flares, it is essential to study the three-dimensional (3D) structure of magnetic fields and their evolution associated with flares. The coronal imaging observations and field modeling approaches contribute to the solution to a certain degree. For instance, the sigmoid-to-arcade transformation of the coronal loops during flares has been frequently observed, signifying that magnetic fields relax to a more potential state (e.g., Sakurai et al. 1992; Mandrini et al. 2005; Liu et al. 2007; Jing et al. 2007). A comparison of the nonlinear force-free (NLFF) fields before and after the eruption shows that magnetic energy and relative helicity decreased after the eruption (Bleybel et al. 2002).

With the aid of high-resolution and high-accuracy vector magnetogram data from the recently launched *Hinode* satellite (Kosugi et al. 2007) and the advanced nonlinear force-free field modeling techniques (e.g., Wiegelmann 2008), we are currently in a good position to make advances to address this issue. In this Letter, we investigate the altitude variation of the nonpotentiality of the magnetic fields associated with the 4B/X3.4 flare of 2006 December 13 with *Hinode* vector magnetograms. The changes of the sunspot structure during the flare are studied with *Hinode* high-cadence G-band observations.

2. DATA SETS AND NONLINEAR FORCE-FREE MODELING OF CORONAL MAGNETIC FIELDS

The 4B/X3.4 flare we discuss in this Letter occurred in NOAA active region 10930 and peaked in the *GOES* soft X-ray at 02:40 UT on 2006 December 13. The G-band (430 nm) observations were obtained with the Broadband Filter Imager (BFI) of Solar Optical Telescope (SOT; Tsuneta et al. 2007) on board *Hinode* with a 2 minute cadence. Since the active region is not located at the center of the solar disk, the images are warped onto a heliographic grid so that they appear as they would had they been at the disk center. The Spectro-Polarimeter

¹ Center for Solar-Terrestrial Research, New Jersey Institute of Technology, Newark, NJ 07102; jj4@njit.edu, haimin@flare.njit.edu.

² Big Bear Solar Observatory, 40386 North Shore Lane, Big Bear City, CA 92314.

³ Max-Planck-Institut für Sonnensystemforschung (MPS), Max-Planck-Strasse 2, 37191 Katlenburg-Lindau, Germany; wiegelmann@linmpi.mpg.de.

⁴ National Astronomical Observatory of Japan, 2-21-1 Osawa, Mitaka, Tokyo 181-8588, Japan; suematsu@solar.mtk.nao.ac.jp.

⁵ High Altitude Observatory, National Center for Atmospheric Research, P.O. Box 3000, Boulder, CO 80307; kubo@ucar.edu. The National Center for Atmospheric Research is sponsored by the National Science Foundation.

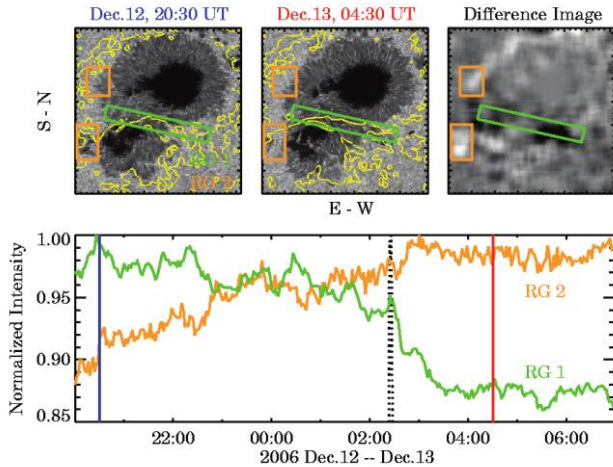


FIG. 1.—*Top panels:* *Hinode* G-band images taken before (*left*) and after (*middle*) the flare, and the difference image (*right*). The contours show magnetic PILs. The central darkening region (RG1) around the flaring magnetic PIL and a peripheral brightening region (RG2) are marked with the green and yellow boxes, respectively. The FOV is $90'' \times 90''$. *Bottom panel:* Normalized time variation of the total G-band intensities in area RG1 (*green*) and RG2 (*yellow*). The blue and red vertical lines denote the times of the vector magnetograms used for 3D extrapolation. The dotted vertical curve is the time derivative of *GOES* X-ray flux.

(SP) of SOT obtained Stokes profiles of two magnetically sensitive Fe lines at 630.15 and 630.25 nm. Photospheric vector magnetograms were obtained based on the assumption of the Milne-Eddington atmosphere. The vector magnetograms taken in two time bins, 20:30–21:33 UT on 2006 December 12 and 4:30–5:36 UT on 2006 December 13, are used as the boundary conditions to extrapolate the coronal magnetic fields before and after the flare. The 180° ambiguity in the vector magnetograms is resolved using the “minimum energy” algorithm that simultaneously minimizes both the electric current density and the field divergence (Metcalf 1994). The magnetograms are rebinned 2×2 to $0.63'' \text{ pixel}^{-1}$. The dimensions of the simulation box are $320 \times 320 \times 256 \text{ pixel}^3$, which correspond to $150 \times 150 \times 120 \text{ Mm}^3$. The potential fields were computed with the Green’s function method (Metcalf et al. 2008). The magnetogram data and the potential fields were prepared by the NLFFF consortium (Schrijver et al. 2008). The details of the data preparation including remapping and disambiguation are described by Schrijver et al. (2008).

In order to reduce the effect of the Lorentz force acting in the photosphere, the rebinned photospheric vector magnetograms have been preprocessed (including spatial smoothing) using a method devised by Wiegmann et al. (2006). The preprocessing routine minimizes a 2D functional of quadratic form $L_{\text{prep}} = \mu_1 L_1 + \mu_2 L_2 + \mu_3 L_3 + \mu_4 L_4$. The L_1 and L_2 terms contain force-free and torque-free consistency integrals, the L_3 term controls how close the preprocessed data are compared to the original magnetogram (noise level), and the L_4 term controls the smoothing. In this case, $\mu_1 = \mu_2 = 1$, $\mu_3 = 0.001$, and $\mu_4 = 0.01$.

The NLFF fields are computed with the “optimization method” (Wheatland et al. 2000) as implemented by Wiegmann (2004). This method involves minimizing a joint measure

(L) for the normalized Lorentz force and the divergence of the field throughout the volume of interest V :

$$L = \frac{1}{V} \int_V [\omega_f(\mathbf{r}) B^{-2} |(\nabla \times \mathbf{B}) \times \mathbf{B}|^2 + \omega_d(\mathbf{r}) |\nabla \cdot \mathbf{B}|^2] dV, \quad (1)$$

where $B = |\mathbf{B}|$ and ω_f and ω_d are weighting functions for the force and divergence terms, respectively. The weighting functions have been chosen $\omega_f = \omega_d = 1$ in the volume except for a boundary layer of 32 points toward the lateral and top boundary of the computational domain. In the boundary layers, ω_f and ω_d drop from 1 to 0 with a cosine profile (see Wiegmann 2004 for details). The force-free equations are solved with the magnetic field vector prescribed in the photosphere as boundary condition.

3. CALCULATION OF MAGNETIC SHEAR

In this work, the magnetic shear θ is defined as the azimuth difference between the extrapolated NLFF magnetic field and the potential field. In each pixel i ,

$$\theta_i = \cos^{-1} \frac{\mathbf{B}_i^N \cdot \mathbf{B}_i^p}{B_i^N B_i^p}, \quad (2)$$

where $B_i = |\mathbf{B}_i|$, and the superscripts N and p represent the NLFF field and the potential field, respectively.

At each altitude, we calculate the weighted mean shear θ_w (Wang et al. 1994) and the total magnetic shear $\theta_w B$ as follows (both provide a quantitative description of the nonpotentiality of the magnetic field):

$$\theta_w = \frac{\sum (B_i^N \theta_i)}{\sum B_i^N}, \quad (3)$$

$$\theta_w B = \theta_w \sum B_i^N = \sum (B_i^N \theta_i), \quad (4)$$

where the sum is performed over all the pixels in a region.

4. RESULTS

In Figure 1 the top row compares the sunspot structure shown in the G-band images taken before (*left*) and after (*middle*) the X3.4 flare. The contours show the magnetic PILs from the SP line-of-sight magnetograms. The alignment between the G-band and the SP images is performed by manually aligning the spots and network structures. In their difference image (*right*), we can identify the dark patches in the central region surrounded by less obvious bright patches. The dark patches correspond to the areas of the darkening inner penumbra, whereas the bright patches correspond to the areas of the decaying peripheral penumbra. To better illustrate the changes of sunspot structure, the central darkening region (RG1) around the flaring magnetic PIL and a peripheral brightening region (RG2) are marked with the green and yellow boxes, respectively. The bottom panel shows the time variation of total G-band intensities in RG1 and in RG2 over a period of ~ 11 hr around the time of the flare. The blue and red vertical lines refer to the starting times of the SP scanning observations before and after

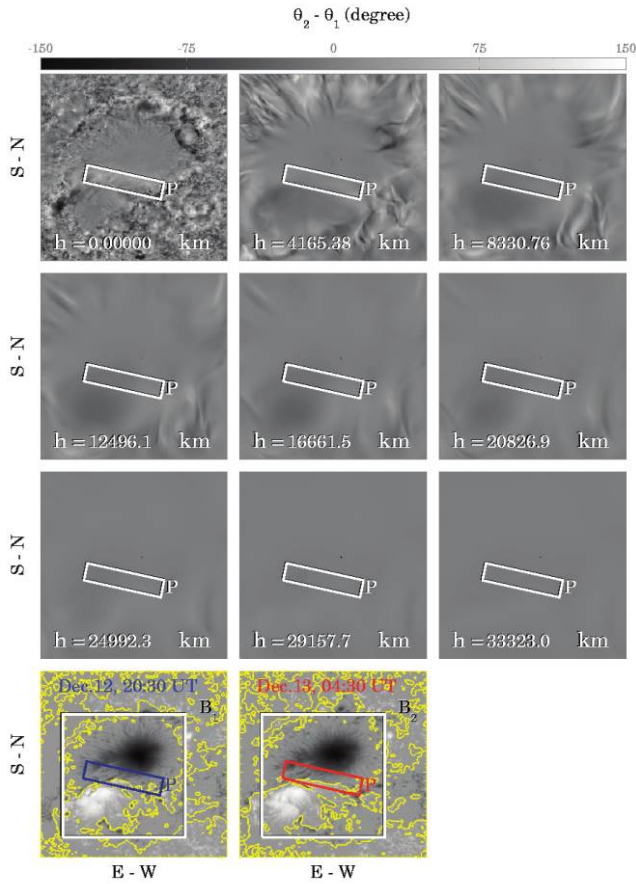


FIG. 2.—*Top three rows:* Shear-difference images $\theta_2 - \theta_1$ at progressively higher altitude, where the subscripts 1 and 2 refer to two time bins of the SP vector magnetograms taken before and after the flare, respectively. The magnitude of $\theta_2 - \theta_1$ in each pixel is indicated by the gray-scale bar. *Bottom row:* Line-of-sight magnetograms taken before (*left*) and after (*right*) the flare. The contours show the magnetic PILs. The FOV is $140'' \times 140''$. The area P close to the magnetic PILs is marked with the rectangles. The large square boxes are drawn to mark the FOV of the G-band images shown in Fig. 1.

the flare, between which there is an 8 hr time interval. The peak time of the flare nonthermal emission is indicated by the time derivative of *GOES* X-ray flux (*dotted vertical spike*). For a direct comparison, all these data are normalized to their maximum value. Evidently, the intensity in RG1 decreases by $\sim 12\%$ within the interval of two time bins while the intensity in RG2 shows relatively little change, $\sim 6\%$. It was observed that, prior to the flare, three emerging flux regions appeared between the two umbrae as well as in the area west of that (Kubo et al. 2007). Parts of the emerging flux merged into the adjacent penumbra enclosed with RG1, which may explain the intensity decrease in this area.

In Figure 2, the top three rows show a sequence of the shear-difference images $\theta_2 - \theta_1$ at progressively higher altitude, where the subscripts 1 and 2 refer to two time bins of the SP vector magnetograms before and after the flare, respectively. The magnitude of $\theta_2 - \theta_1$ in each pixel is indicated by the gray-scale bar. The two panels in the bottom row are the preflare (*left*) and postflare (*right*) line-of-sight magnetograms, respectively. The contours show the magnetic PILs. The large square boxes are drawn to mark the field-of-view (FOV) of the G-band images shown in Figure 1. By comparing the line-of-sight

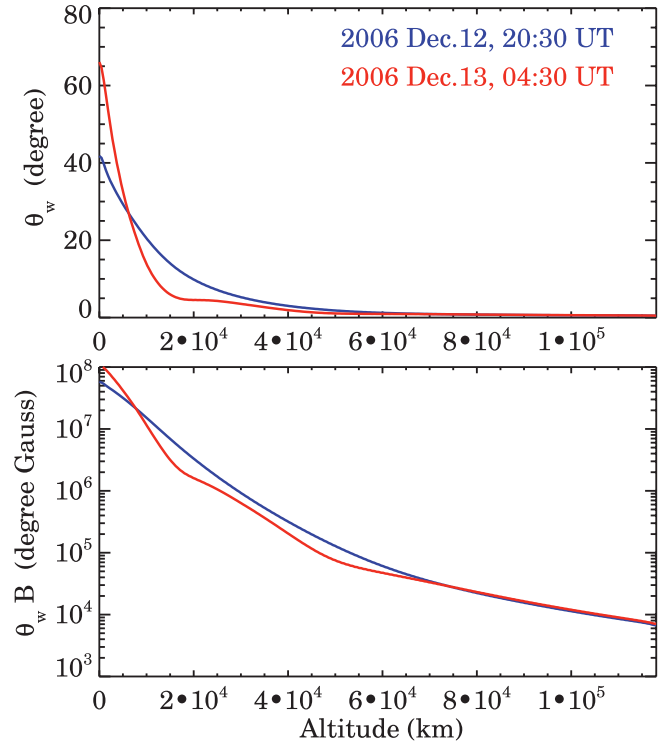


FIG. 3.—Weighted mean shear θ_w (*top*) and the total magnetic shear $\theta_w B$ (*bottom*) of area P (defined in Fig. 2) as a function of altitude for two time bins. The step size of altitude is ~ 0.46 Mm. *Blue:* Before the flare. *Red:* After the flare.

magnetograms and the shear-difference image at the photosphere boundary ($h = 0$), we can see an increase in magnetic shear in an area P near the flaring magnetic PIL. This area P is marked by the small rectangles. Since the development of shear around the magnetic PIL is more essential for the flare occurrence, θ_w and $\theta_w B$ in the area P at two time bins are specifically calculated for a quantitative comparison, which is shown in Figure 3.

In Figure 3 we plot the θ_w (*top*) and $\theta_w B$ (*bottom*) in the area P as a function of altitude for two time bins. As mentioned, both θ_w and $\theta_w B$ can provide a quantitative description of the nonpotentiality of the local area. We see that (1) from the photosphere boundary to an altitude of ~ 8 Mm, the magnetic shear in an area around the magnetic PILs increases after the flare; (2) from ~ 8 to ~ 70 Mm, the shear in this area decreases after the flare; and (3) beyond ~ 70 Mm, both pre- and postflare fields approach potential.

5. SUMMARY

Hinode G-band observations reveal that the sunspot structure undergoes some changes during the X3.4 flare of 2006 December 13. The most conspicuous change is the darkening of the central feature near the flaring magnetic PIL, probably as a result of the continuing flux emergence at this region. The abrupt penumbral decay associated with major flares was first observed by Howard (1963) and recently by Wang et al. (2004), Deng et al. (2005), Liu et al. (2005), and Chen et al. (2007). Compared with the previous observations, the duration of this observation (~ 11 hr) is 2–3 times longer. Therefore, we find that although the change rate peaks in association with the flare, the trend of change is persistent. That is, the intensity changes

start even several hours prior to the flare, achieve the maximum change rate immediately after the flare, and are complete ~ 1 hr after the flare emission ceased. The intensity changes in the peripheral penumbrae are not as obvious as that in the central feature. Comprehensive quantitative study of decaying penumbral structure will be presented in a future paper.

We compare the height variations of the shear parameters calculated in the pre- and postflare NLFF fields, and find that 8 Mm appears to be a critical height, below which the non-potentiality increases after the flare and above which to a height of ~ 70 Mm the field is relaxed to a more potential state. As mentioned, previous observations of the photosphere magnetic field show that magnetic shear can increase after the flare (e.g., Ambastha et al. 1993; Chen et al. 1994; Wang et al. 1994; Schmieder et al. 1994). It seems puzzling because shear increase signifies energy buildup, rather than release for energizing flares. This work, based on the shear evaluation in 3D magnetic field, may resolve the previous observational paradox: the magnetic shear may increase in a local area near the flaring magnetic PIL due to the emerging flux regions, but, at higher altitudes, magnetic fields are relaxed. In particular, it appears likely that the energy release process happens at the altitude ranging from ~ 8 Mm to ~ 70 Mm.

It is worth noting that the ongoing flux emergence not only

causes an increase in the magnetic shear at low altitude (< 8 Mm), but also causes an increase in free energy by $\sim 5\%$ from the preflare fields to the postflare fields (Schrijver et al. 2008). Presumably the flare might only release some of the new energy introduced by the flux emergence. NOAA 10930 is a flare-productive active region. Its energy buildup and release process requires magnetic field observations with higher cadence. The 8 hr interval between the SP magnetograms is certainly too long to address this issue.

We thank Brian Welsch and the referee for the valuable comments. *Hinode* is a Japanese mission developed and launched by ISAS/JAXA, collaborating with NAOJ as a domestic partner, and NASA and STFC (UK) as international partners. The authors thank the NLFFF consortium for preparing and providing the data. This work was partly carried out at the NAOJ *Hinode* Science Center, which is supported by the Grant-in-Aid for Creative Scientific Research "The Basic Study of Space Weather Prediction" from MEXT, Japan (Head Investigator: K. Shibata), generous donations from Sun Microsystems, and NAOJ internal funding. J. J. and H. W. were supported by the NSF under grants ATM 07-16950 and ATM 05-48952, and NASA under grant NNX0-7AH78G. T. W. was supported by DLR-grant 50 OC 0501.

REFERENCES

- Ambastha, A., Hagyard, M. J., & West, E. A. 1993, *Sol. Phys.*, 148, 277
 Bleybel, A., Amari, T., van Driel-Gesztelyi, L., & Leka, K. D. 2002, *A&A*, 395, 685
 Chen, J., Wang, H., Zirin, H., & Ai, G. 1994, *Sol. Phys.*, 154, 261
 Chen, W., Liu, C., Song, H., Deng, N., Tan, C., & Wang, H. 2007, *Chinese J. Astron. Astrophys.*, 7, 733
 Deng, N., Liu, C., Yang, G., Wang, H., & Denker, C. 2005, *ApJ*, 623, 1195
 Howard, R. 1963, *ApJ*, 138, 1312
 Jing, J., Lee, J., Liu, C., Gary, D. E., & Wang, H. 2007, *ApJ*, 664, L127
 Kosovichev, A. G., & Zharkova, V. V. 2001, *ApJ*, 550, L105
 Kosugi, T., et al. 2007, *Sol. Phys.*, 243, 3
 Kubo, M., et al. 2007, *PASJ*, 59, S779
 Liu, C., Deng, N., Liu, Y., Falconer, D., Goode, P. R., Denker, C., & Wang, H. 2005, *ApJ*, 622, 722
 Liu, C., Lee, J., Gary, D. E., & Wang, H. 2007, *ApJ*, 658, L127
 Mandrini, C. H., Pohjolainen, S., Dasso, S., Green, L. M., Démoulin, P., van Driel-Gesztelyi, L., Copperwheat, C., & Foley, C. 2005, *A&A*, 434, 725
 Metcalf, T. R. 1994, *Sol. Phys.*, 155, 235
 Metcalf, T. R., et al. 2008, *Sol. Phys.*, 247, 269
 Moore, R. L., Sterling, A. C., Hudson, H. S., & Lemen, J. 2001, *ApJ*, 552, 833
 Sakurai, T., Shibata, K., Ichimoto, K., Tsuneta, S., & Acton, L. W. 1992, *PASJ*, 44, L123
 Schmieder, B., et al. 1994, *Sol. Phys.*, 150, 199
 Schrijver, C., et al. 2008, *ApJ*, 675, 1637
 Sudol, J. J., & Harvey, J. W. 2005, *ApJ*, 635, 637
 Tsuneta, S., et al. 2007, *Sol. Phys.*, submitted
 Wang, H. 1992, *Sol. Phys.*, 140, 85
 ———. 2006, *ApJ*, 649, 490
 Wang, H., Ewell, M. E., Jr., Zirin, H., & Ai, G. 1994, *ApJ*, 424, 436
 Wang, H., Liu, C., Qiu, J., Deng, N., Goode, P. R., & Denker, C. 2004, *ApJ*, 601, L195
 Wheatland, M. S., Sturrock, P. A., & Roumeliotis, G. 2000, *ApJ*, 540, 1150
 Wiegelmann, T. 2004, *Sol. Phys.*, 219, 87
 ———. 2008, *J. Geophys. Res.*, 113, A03S02, doi:10.1029/2007JA012432
 Wiegelmann, T., Inhester, B., & Sakurai, T. 2006, *Sol. Phys.*, 233, 215